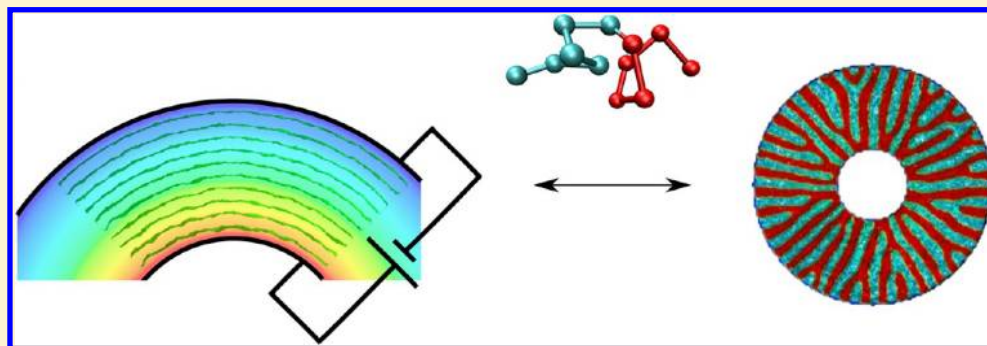# Block Copolymer Ordering in Cylindrical Capacitors

U. Welling,*,[†] M. Müller,[†] H. Shalev,[‡] and Y. Tsori[‡]

[†]Institut für Theoretische Physik, Georg-August-Universität, 37077 Göttingen, Germany

[‡]Department of Chemical Engineering and The Ilse Katz Institute for Nanoscale Science and Technology, Ben-Gurion University of the Negev, 84105 Beer-Sheva, Israel

ABSTRACT: We investigate the morphologies of block copolymers confined in the region between two concentric and charged cylinders. The relative stability of a concentric lamellar phase compared to one where the lamellae are oriented in the radial direction is determined from the competition between long-range elastic and electrostatic forces. We find in weak and strong segregation and by single-chain-in-mean-field simulations that under sufficiently strong voltage difference there is a phase transition from concentric to radial lamellae containing defects. Above a threshold voltage the block copolymer melt develops an interfacial instability at a finite wavelength.

1. INTRODUCTION

Block copolymers (BCPs) self-assemble to numerous phases with periodicities on the nanoscale.[1] Because of their potential applications, a considerable effort has been invested in finding ways to control the orientation of these phases and to reduce the number of their defects. Methods such as shear flow, confinement to thin films and the use of external magnetic and electric fields have been shown to be useful.[2] Electric fields are particularly appealing since at fixed potentials they increase favorably with decreasing system size. Because of its importance, the effects of electric fields on BCPs have been studied both theoretically and experimentally.[3−17] These works deal with spatially uniform fields and in such fields there is a symmetry of rotation around the axis of the field. This degeneracy means that the field does not remove all the defects in the system, leading to the possibility of grains with different orientations.

In this work we extend the previous effort and look in details on the case of spatially nonuniform electric fields. Specifically, we calculate the phases of BCPs near a charged cylinder where the field decays in the radial direction as the distance from symmetry axis increases. The competition between the elastic and electrostatic energies leads to changes in the BCP orientation and even to phase transitions. An understanding of the competition between these long-range volume forces is essential for fundamental research and may also be useful for applications where BCP phases need to be perfectly registered on a substrate.[18]

As we show below, interesting phenomena occur at weak and intermediate segregations, where significant bending of domains can occur. At these temperatures the BCP domains are only partially segregated and the chains are not fully stretched, and hence the external field can substantially influence the polymer morphology. Accordingly, we use a Ginzburg–Landau approach for a melt close to the order–disorder temperature (ODT), strong segregation claculation at high incompatibilities and single-chain-in-mean-field (SCMF) Monte Carlo simulation for intermediate segregations.[19,20]

2. WEAK SEGREGATION CALCULATIONS

We consider block polymers composed of N_A monomers of type A and N_B monomers of type B. Close enough to the critical point the BCP free energy can be given as an expansion in powers of the deviation of the composition from its average value[21−23]

$$\frac{H_{pol}}{k_B T} = \int \left[\frac{1}{2}\tau\phi^2 + \frac{1}{2}h(\nabla^2\phi + q_0^2\phi)^2 + \frac{u}{4!}\phi^4 \right] d\mathbf{r} \tag{1}$$

Here $\phi(r) = c\bar{N}^{1/4}(\phi_A - f)$ is the order parameter, where ϕ_A is the local volume fraction of A monomers, $f = \langle\phi_A\rangle$ is its spatial average, $\bar{N} = (R_e^3\rho)^2$, $R_e^2 = Nb^2$ is the mean squared
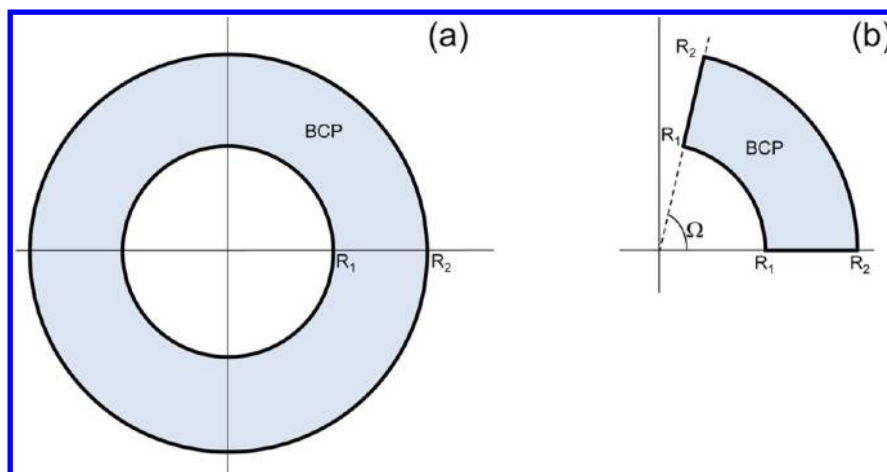
Figure 1. Block copolymer melt confined in a cylindrical capacitor. (a) Copolymers are found in the shaded annular region confined between two charged and concentric cylinders. In geometry b, useful for numerical computations, the copolymers are confined into a wedge of opening angle Ω.

end-to-end distance, b is the statistical segment length, and ρ is the number of polymer chains per unit volume. The spatial coordinate $\mathbf{r}$ is scaled by R_e. In addition,

$$\tau = \frac{2}{c^2}(\chi_s N - \chi N), \quad u = \lambda \bar{N}^{-1/2} \tag{2}$$

where χ is the Flory−Huggins interaction parameter, $\chi \sim 1/T$, and χ_s is its spinodal value. q_0 is the wavenumber describing the BCP periodicity; $d_0 = 2\pi/q_0$ is the typical length in the system.[23] We restrict our attention to symmetric BCP compositions $f = 1/2$ where $c = 1.1019$, $\chi_s N = 10.495$, $\lambda = 106.18$, $q_0^2 = 6x^*$, $h = 1/(24x^*)$, $x^* = 3.7852$, and τ is negative.

The electrostatic energy is given by the integral

$$\frac{H_{es}}{k_B T} = -M \int \tilde{\varepsilon}(\phi(\mathbf{r})) \tilde{\mathbf{E}}^2 \, d\mathbf{r}$$

$$M = \frac{R_e \varepsilon_0 \psi_0^2}{2 k_B T} \tag{3}$$

Here the dielectric constant is scaled by the vacuum permittivity ε_0 and varies locally leading to $\tilde{\varepsilon} = \varepsilon/\varepsilon_0$. The dimensionless parameter M measure the importance of the electrostatic energy stored in a volume of size $\sim R_e^3$ compared to the thermal energy. The dimensionless electric field $\tilde{\mathbf{E}}$ in (3) is scaled by the typical electric field $E_0 = \psi_0/R_e$, where ψ_0 is the electric potential defined below. The constitutive relation between dielectric constant and composition is assumed to be linear:

$$\varepsilon(\phi_A) = \varepsilon_0 \varepsilon_A \phi_A + (1 - \phi_A) \varepsilon_0 \varepsilon_B \tag{4}$$

$$= \bar{\varepsilon} + \Delta\varepsilon \frac{\varepsilon_0 \phi}{c N^{1/4}} \tag{5}$$

where ε_A and ε_B are the dimensionless permittivities of the A and B polymers, the average permittivity is $\bar{\varepsilon} = \varepsilon_0(\varepsilon_A f + \varepsilon_B(1 - f))$ and the dielectric contrast is $\Delta\varepsilon = \varepsilon_A - \varepsilon_B$.

The BCP melt is placed inside a concentric capacitor as is shown in Figure 1. The potential of the inner cylinder with radius R_1 is ψ_0 whereas it vanishes on the outer cylinder with radius R_2. The typical electric breakdown of polymers occurs for fields ≥ 200 $V/\mu m$.[10] In a concentric capacitor the highest electric field is $E_{max} \simeq \psi/R_1$ and this sets a higher limit on the possible potential. We write the total free energy as

$H_{tot} = H_{pol} + H_{es}$ and use the variational principle to write the Euler−Lagrange equation:

$$\frac{1}{k_B T h} \frac{\delta H_{tot}}{\delta \phi} = \nabla^4 \phi + 2 q_0^2 \nabla^2 \phi + \left(\frac{\tau}{h} + q_0^4\right) \phi + \frac{u}{6h} \phi^3$$
$$- \frac{M \Delta\varepsilon}{h c \bar{N}^{1/4}} \tilde{E}^2 = 0 \tag{6}$$

where the dielectric contrast is defined as $\Delta\varepsilon = \varepsilon_A - \varepsilon_B$. The boundary conditions for ϕ

$$\nabla^2 \phi + q_0^2 \phi = 0$$

$$\nabla(\nabla^2 \phi + q_0^2 \phi)\cdot \hat{n} = 0 \tag{7}$$

are applied on the bounding surfaces. For a one-dimensional system these are calculated at the lower and upper bound of the domain and hence there are four equations. Here $\hat{n}$ is the unit vector normal to the surfaces. The electric field satisfies Laplace's equation

$$\nabla \cdot [\varepsilon(\phi(\mathbf{r})) \mathbf{E}(\mathbf{r})] = 0 \tag{8}$$

and it is related to the electric potential ψ via $\mathbf{E} = -\nabla\psi$, where the boundary conditions for the potential are

$$\psi(r = R_1) = \psi_0, \quad \psi(r = R_2) = 0 \tag{9}$$

The above equations describe the equilibrium distribution of the two fields: polymer density and electric field.

2.1. Radial and Concentric Lamellae in the Absence of External Potential. Before solving the complete system state it is instructive to look at the stability of ordered phases even in the absence of an external potential. In order to understand the influence of an external field we need to first look at the BCP phases in its absence. Below we consider three possible morphologies: radial lamellae, concentric lamellae, and the disordered phase.

● *Radial Lamellae.* We want to calculate the free energy of lamellae, which extend in the radial direction, namely of lamellae whose order parameter is

$$\phi(\mathbf{r}) = \phi_0 \cos\left(\frac{2\pi\theta}{\theta_0}\right) \tag{10}$$

Here θ is the azimuthal angle, $\phi_0 = (-8\tau/\mu)^{1/2}$ is the amplitude of the bulk "perfect" sinusoidal modulations, and θ_0 is a variational parameter to be found below. The BCP are confined to a wedge of opening angle Ω; in the case of $\Omega = 2\pi$ the symmetry of the system requires that $n\theta_0 = 2\pi$ where n is an integer number. We carry out the integral (1) in a cylindrical coordinate system. The resulting energy per unit length of the cylinder is

$$\frac{H_{\text{pol}}^{\text{rad}}(\theta_0)}{k_{\text{B}}T} = -\frac{\Omega\tau}{u}\left(\frac{b}{\theta_0^2} + c + \frac{a}{\theta_0^4}\right) \tag{11}$$

where

$$a = 16\pi^4 h\left(\frac{1}{R_1^2} - \frac{1}{R_2^2}\right)$$

$$b = 16\pi^2 hq_0^2 \ln(R_1/R_2)$$

$$c = (R_2^2 - R_1^2)(hq_0^4 + \tau/2) \tag{12}$$

Therefore, the "optimal" value of θ_0 is given by $\theta_0^2 = -2a/b$ (which is positive because $b < 0$). We substitute this value back into the free energy and express it as

$$\frac{H_{\text{pol}}^{\text{rad}}}{k_{\text{B}}T} = -\frac{\Omega\tau hq_0^2}{u}$$
$$\times \left[-4(q_0R_1)^2 \frac{X^2[\ln X]^2}{X^2 - 1} + \frac{1}{2}(X^2 - 1)(\overline{\tau} + 2(q_0R_1)^2)\right] \tag{13}$$

$$X \equiv R_2/R_1, \qquad \overline{\tau} \equiv \frac{\tau R_1^2}{hq_0^2} \tag{14}$$

This energy evidently depends on the reduced temperature $\overline{\tau}$ and on the geometry parameter X, the ratio between the two radii. Note that the energy density $H_{\text{pol}}^{\text{rad}}/(\Omega(R_2^2 - R_1^2)/2)$ can be positive or negative, but it is always larger than the bulk energy density $-\tau^2/u$.

Stability of Radial Lamellae vs Disorder. The energy of the disordered melt is zero and therefore radial lamellae are stable when $H_{\text{rad}}^{\text{pol}} < 0$. As a function of X, $H_{\text{rad}}^{\text{pol}}(X)$ decreases to negative values until, at large enough values of X, it increases and then becomes positive. The value of X, at which $H_{\text{rad}}^{\text{pol}} = 0$, decreases with decreasing value of $|\overline{\tau}|$, i.e., closer to the ODT point. Conversely, one may want to look at the value of $\overline{\tau}$, at which radial lamellae coexist with a disordered morphology. Denoting this value as $\overline{\tau}_c$ we find that

$$\overline{\tau}_c = 2(q_0R_1)^2\left[\left(\frac{2X\ln X}{X^2 - 1}\right)^2 - 1\right] \tag{15}$$

Both sides of this equation are negative. Radial lamellae are favored over disorder if $\overline{\tau} > \overline{\tau}_c$, i.e., if χN is close enough to $\chi_s N$. For too large values of χN the energy penalty in the splay is too large and the disorder phase has a lower free energy. Interestingly, if the ratio between the two radii is very large, $X \to \infty$, we find that radial lamellae occur if $|\overline{\tau}| < 2(q_0R_1)^2$.

● *Concentric Lamellae.* To calculate the polymer part of the free energy of concentric lamellae we substitute the composition profile $\phi = \phi_0 \cos(q_0(r - R_1))$ in (1) and carry out the integration. In order to isolate the effect of bending from the influence of a possible mismatch between the lamellar

period $2\pi/q_0$ and the spacing between the cylinders $R_2 - R_1$ we assume that $q_0R_1 = n\pi$ and $q_0R_2 = m\pi$, with integers n and m. The result is

$$\frac{H_{\text{pol}}^{\text{con}}}{k_{\text{B}}T} = \frac{\Omega\tau}{u}\left[2hq_0^2 \ln(R_2/R_1) + \frac{1}{2}\tau(R_2^2 - R_1^2)\right.$$
$$\left. + 2hq_0^2(Ci(2q_0R_1) - Ci(2q_0R_2))\right] \tag{16}$$

Here $Ci(z) = -\int_z^\infty \cos(t)/t\, dt$ is the cosine integral. In the limit of large radii, $q_0R_1 \gg 1$ and $q_0R_2 \gg 1$, the cosine integrals vanish and we have

$$\frac{H_{\text{pol}}^{\text{con}}}{k_{\text{B}}T} = -\frac{\Omega\tau hq_0^2}{u}\left[2\ln(X) + \frac{1}{2}\overline{\tau}(X^2 - 1)\right] \tag{17}$$

Stability of Concentric Lamellae vs Disorder. The plot of $H_{\text{pol}}^{\text{con}}(X)$ for $X \geq 1$ decreases from zero to negative values before it goes up at sufficiently large values of X. The larger the value of $|\overline{\tau}|$ (farther below the ODT temperature), the sooner the plot increases. The value of X at which $H_{\text{pol}}^{\text{con}}$ vanishes decreases accordingly. One may express the value of $\overline{\tau}$, $\overline{\tau}_c$, at which concentric lamellae have the same energy as the disordered phase,

$$\overline{\tau}_c = -\frac{4\ln(X)}{X^2 - 1} \tag{18}$$

If $\overline{\tau}$ is smaller (more negative) than $\overline{\tau}_c$ then the bending energy is too high and the disordered phase is more stable than concentric lamellae.

Stability of concentric vs radial lamellae. In order to find the relative stability of radial and concentric lamellae we compare the energy difference from (13) and (17):

$$\frac{H_{\text{pol}}^{\text{rad}} - H_{\text{pol}}^{\text{con}}}{k_{\text{B}}T} = -\frac{\Omega\tau hq_0^2}{u}\left[-4(q_0R_1)^2 \frac{X^2[\ln X]^2}{X^2 - 1}\right.$$
$$\left. + (X^2 - 1)(q_0R_1)^2 - 2\ln(X)\right] \tag{19}$$

The sign of this difference between the free energies of the two phases depends on the sign of the squared brackets, i.e., the boundary between radial and concentric phases depends only on the geometry and not on the incompatibility $\overline{\tau}$. A graphical representation of the phase diagram is shown in Figure 2.

2.2. The Electrostatic Energy. We now add the electrostatic energy of the various possible morphologies. For simplicity in the following derivation and without loss of generality we assume that the inner cylinder of radius R_1 has a fixed charge per unit area, σ_0. The electric field follows from Gauss' theorem and is given by

$$\mathbf{E}(r, \theta) = \frac{\sigma_0 R_1}{\varepsilon(\phi(r, \theta))r}\hat{\mathbf{r}} \tag{20}$$

This expression holds for BCP in *both* the radial and concentric lamellar phases. In order to know the potential difference across the inner and outer cylinders one needs to integrate this field from R_1 to R_2. This is very simple for radial lamellae but is more cumbersome analytically for concentric lamellae.

2.2.1. Concentric Lamellae. Here
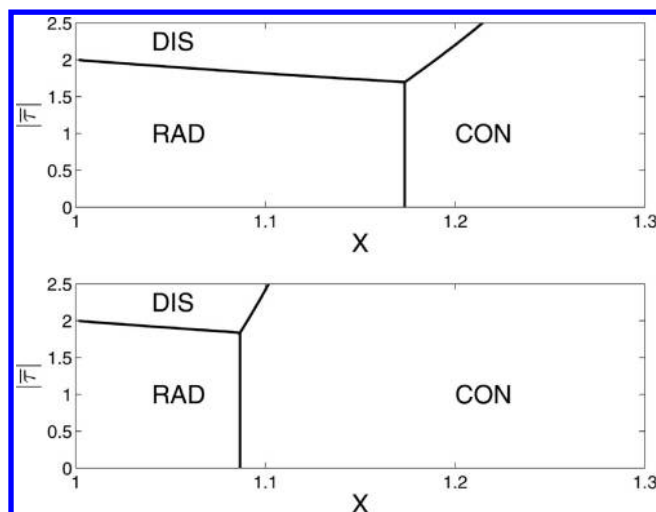
$$\phi = \phi_0 \cos(q_0(r - R_1)) \tag{21}$$

Figure 2. Analytical phase diagram of radial and concentric lamellae confined in a cylindrical capacitor in the absence of electric field. The boundaries between phases are taken from eqs 13,17. Key: (a) $q_0 R_1$ = 10 and (b) $q_0 R_1$ = 20.

The electrostatic energy per unit length of the cylinders is

$$\frac{H_{es}^{con}}{k_B T} = \frac{\Omega \sigma_0^2 R_1^2}{2\varepsilon_0 k_B T} \int_{R_1}^{R_2} \frac{1}{\tilde{\varepsilon}(\phi) r} \, dr$$

When we expand $1/\tilde{\varepsilon}(\phi)$ as

$$\frac{1}{\tilde{\varepsilon}(\phi)} \simeq \frac{1}{\bar{\varepsilon}}\left[1 - \frac{\Delta\varepsilon}{c\bar{N}^{1/4}\bar{\varepsilon}}\phi + \left(\frac{\Delta\varepsilon}{c\bar{N}^{1/4}\bar{\varepsilon}}\right)^2 \phi^2\right] \tag{22}$$

we obtain

$$\frac{H_{es}^{con}}{k_B T} \simeq \frac{\Omega(\sigma_0 R_1)^2}{2\varepsilon_0 k_B T}\left\{ \frac{\ln(R_2/R_1)}{\bar{\varepsilon}} \right.$$
$$- \frac{\Delta\varepsilon}{c\bar{N}^{1/4}\bar{\varepsilon}}\phi_0[\cos(q_0 R_1)(Ci(q_0 R_2) - Ci(q_0 R_1))$$
$$+ \sin(q_0 R_1)(Si(q_0 R_2) - Si(q_0 R_1))]$$
$$+ \frac{1}{2\bar{\varepsilon}^3}\left(\frac{\Delta\varepsilon}{c\bar{N}^{1/4}}\right)^2 \phi_0^2[\cos(2q_0 R_1)(Ci(2q_0 R_2)$$
$$- Ci(2q_0 R_1)) + \sin(2q_0 R_1)(Si(2q_0 R_2)$$
$$\left. - Si(2q_0 R_1)) + \ln(R_2/R_1)]\right\} \tag{23}$$

Here the sine integral is given by $Si(x) = \int_0^x \sin(t)/t \, dt$. The linear contribution in ϕ_0 in H_{es}^{con} does not vanish because an exchange of the A and B polymers in the lamellae, equivalent to $\phi_A \to 1 - \phi_A$, does not leaves the system invariant. If the limit $q_0 R_1 \gg 1$ holds, eq 23 reduces to H_{es}^{dis}, where

$$\frac{H_{es}^{dis}}{k_B T} = \frac{\Omega \sigma_0^2 R_1^2}{2\varepsilon_0 k_B T}\frac{\ln(R_2/R_1)}{\bar{\varepsilon}} \tag{24}$$

is the electrostatic energy of the disordered melt.

2.2.2. Radial Lamellae. Close to the ODT (critical) point we have

$$\phi = \phi_0 \cos\left(\frac{2\pi\theta}{\theta_0}\right) \tag{25}$$

The electrostatic energy per unit length of the cylinder is

$$\frac{H_{es}^{rad}}{k_B T} = \frac{1}{2\varepsilon_0 k_B T}\int_0^\Omega d\theta \int_{R_1}^{R_2} \frac{(\sigma_0 R_1)^2}{\bar{\varepsilon}(\phi)} \, dr$$
$$= \frac{(\sigma_0 R_1)^2}{2\varepsilon_0 k_B T}\frac{\ln(R_2/R_1)}{\bar{\varepsilon}} \int_0^\Omega \frac{1}{\bar{\varepsilon} + \frac{\Delta\varepsilon}{c\bar{N}^{1/4}}\phi_0 \cos(2\pi\theta/\theta_0)} \, d\theta \tag{26}$$

In order to be consistent with our previous calculations we use the limit $\bar{\varepsilon} \gg \frac{\Delta\varepsilon}{c\bar{N}^{1/4}}\phi_0$ to expand the denominator in power series. To quadratic order in ϕ_0 we obtain

$$\frac{H_{es}^{rad}}{k_B T} \simeq \frac{\Omega(\sigma_0 R_1)^2}{2\varepsilon_0 k_B T}\frac{\ln(R_2/R_1)}{\bar{\varepsilon}}\left[1 + \frac{1}{2}\left(\frac{\Delta\varepsilon}{c\bar{N}^{1/4}}\phi_0\right)^2\right] \tag{27}$$

In the limit of $\phi_0 \to 0$, eqs 2723 are identical with eq 24, as they should be, because in this limit the system is disordered. The system of radial lamellae is invariant with respect to an interchange of A and B polymers and therefore the linear term $\propto \phi_0$ is absent from (27). Hence, to linear order in ϕ_0 concentric lamellae have lower electrostatic energy than radial ones. This is because a high-dielectric material is found at the inner cylinder, where the electric field is highest. Note that the reversal of the sign of ϕ_0 in (23) ensures that the linear term in ϕ_0 becomes negative. The term quadratic in ϕ_0 in (23), without the "frustration" terms (those depending on the cosine and sine integrals), is identical to the quadratic term in (27).

2.3. Numerical Solution of the Euler−Lagrange Equations. In order to relax the assumption that the polymer morphology can only be "perfectly" radial or concentric lamellae we numerically solved the set of nonlinear eqs 68 subject to the boundary conditions (7) and (9). Figure 3 shows the change of the polymer free energy as the voltage increases from zero (increasing M). As is expected the energy of the radial lamellae increases slowly with M because the electric field distribution in this phase is not very different from its distribution in the disordered melt. However, the energy of
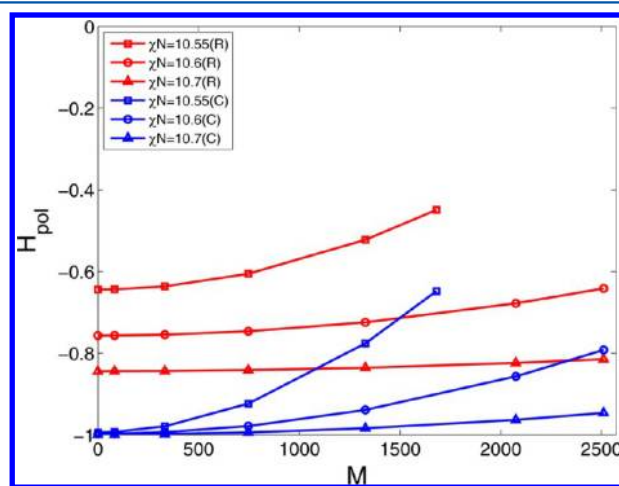

Figure 3. Numerically calculated polymer energies in the radial (H_{pol}^{rad}, R) and concentric (H_{pol}^{con}, C) phases at different values of χN vs M. The energies are averaged over the available volume and scaled by the bulk lamellar energy density $k_B T \tau^2/u$. Unless stated otherwise, in this and in other figures the system size is $R_1 = 20d_0$ and $R_2 = 30d_0$, $\Omega = 12°$.

concentric lamellae increases markedly because the field lines are perpendicular to the lamellae and the cost of "dielectric interfaces" is high.

Figure 4 shows the electrostatic energy of the radial and concentric phases relative to that of the disordered melt.
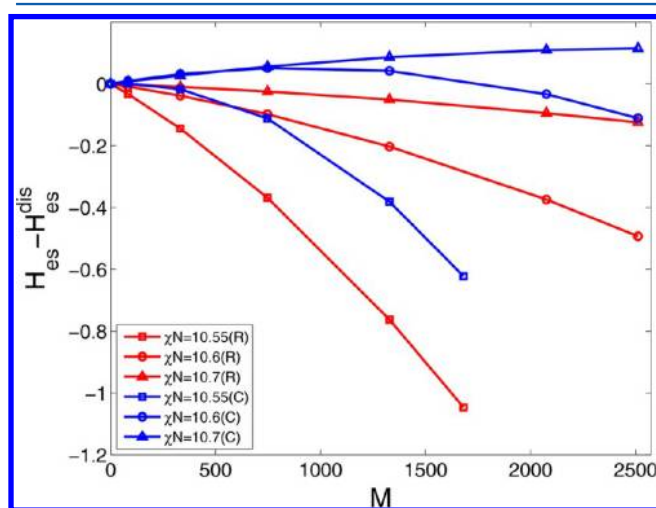

Figure 4. Numerically calculated electrostatic energies in the radial (H_{es}^{rad}, R) and concentric (H_{es}^{con}, C) phases at different values of χN vs M. The energies are averaged over the available volume and scaled by the bulk lamellar energy density τ^2/u and by $k_B T$.

The energy of the radial phase is always lower than that of the disordered melt because the dielectrophoretic effect reduces its energy and there is no cost of dielectric interfaces perpendicular to the field lines. At small voltages, the energy of the concentric lamellae is higher than the energy of the disordered melt because of the cost associated with dielectric interfaces. Only at relatively high values of M does the dielectrophoretic gain overcome this cost and the electrostatic energy begins to decrease with M.

Figure 5 plots the summation of the electrostatic and polymer energies in both phases at different segregations χN. At small values of M (small potentials) the concentric phase is preferred
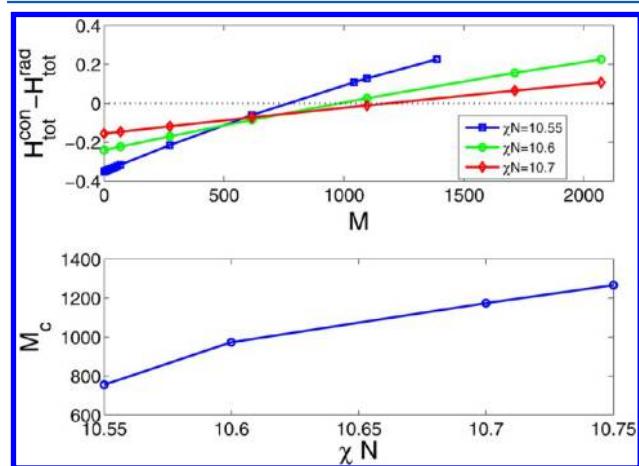

Figure 5. (a) Total energy difference between concentric and radial morphologies with different values of χN vs M. The energies are calculated numerically and normalized by $k_B T \tau^2/u$. Positive values indicate that the radial solution is preferred energetically, while negative values indicate that the concentric phase is preferred. (b) Critical value of M for the transition, M_c, vs the segregation χN.

while at high enough potentials the electric field overcomes the elastic deformations of the polymer and a transition is realized to radial lamellae. The first voltage where this happens is the critical voltage ψ_c (corresponding value M_c). Part b of the figure shows the dependence of M_c on temperature. The higher the segregation the more "stiff" the lamellae are and the more difficult it is to align them in the direction of the external field.

An increase of the electrostatic potential ψ_0, in both the radial and concentric phases, causes an enrichment of the A-type monomers in the region of high electric field (small values of r) for $\Delta\varepsilon > 0$. This enrichment decreases the electrostatic energy and therefore is stronger in high potentials. To quantify this dielectrophoretic behavior we defined $\langle\phi\rangle_n$ for both phases as

$$\langle\phi\rangle_n = \frac{1}{\Omega d_0^2 \phi_0} \int_0^\Omega d\theta \int_{r_n - d_0}^{r_n} \phi(r, \theta) r \, dr,$$

$$r_n = R_1 + n d_0, \qquad n = 1, 2, \dots \qquad (28)$$

Ω is the opening angle we used in the numerical calculations, typically equal to 12° or 30°. For values of r in the range $R_1 \leq r \leq R_1 + d_0/2$ the concentric phase "gains" an electrostatic energy compared to the radial phase, and it "loses" when r is in the range $R_1 + d_0/2 \leq r \leq R_1 + d_0$. But since the electrostatic energy density scales as r^{-2}, the gain is larger than the loss. Plots of $\langle\phi\rangle_n$ are shown in Figure 6 for voltages below and above the critical voltage ψ_c for alignment. Note that a small segregation of A monomers at smaller radii r leads to its depletion from larger radii and hence the curves are decreasing with r.

2.3.1. Defects and Orientational Order Parameter. The lamellae confined in the capacitor are deformed by the electric field. This deformation can be in the radial direction (due to the dielectrophoretic force) or along the azimuthal angle θ. This latter deformation will be related to interfacial undulations below. Figure 7 shows the polymer free energy density in concentric and radial morphologies. While the concentric lamellae are close to ideal, clearly, the radial lamellae are deformed and have defects. These defects allow the polymers to relieve the high strain associated with the splay of radial lamellae and keep a constant lamellar thickness throughout most of the space available to them. The free energy penalty focuses to few points where its density can be as high as twice the free energy density of perfect bulk lamellae (e.g., red regions in Figure 7b). Similar defects are clearly seen in a plot of $\phi(r,\theta)$ in Figure 8 where the wedge is wider.

To quantify the deviation from perfect radial or concentric lamellae we define the following orientational order parameter D

$$D = \frac{1}{q_0 \phi_0} \left\langle \left| \frac{\partial\phi}{\partial\theta} \right| \right\rangle \qquad (29)$$

where $\langle\dots\rangle$ denotes average over the volume available to the BCP. For perfect concentric lamellae $D = 0$ whereas for perfect radial lamellae $\phi = \phi_0 \cos(q_0 \bar{R}\theta)$, where $\bar{R}$ is in the range $R_1 \leq \bar{R} \leq R_2$, and therefore we expect D to be given by $D \simeq 2\bar{R}/\pi$. At small voltages the concentric phase is favorable over the radial phase. As is seen in Figure 9, the concentric phase deforms gradually with increasing values of M until, at $M = M_c$, there is a first-order phase transition to the radial phase. The deformations are larger close to the critical point (ODT) and very small at high values of χN.

2.3.2. Interfacial Instability. An interfacial instability of concentric lamellae can occur if the external field is large enough. Such an instability is shown in Figure 10. The peristaltic-like
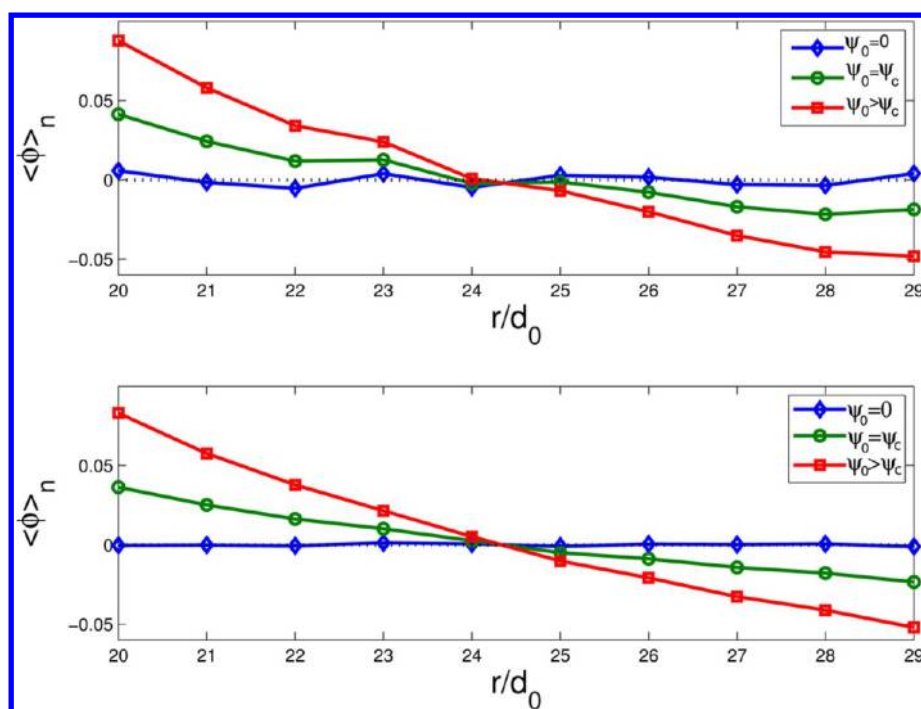
Figure 6. Dielectrophoretic effect in different electric potentials. $\langle\phi\rangle_n$ from 28 for (a) concentric and (b) radial phases. Clearly the segregation of A-monomers near the inner radius grows with increasing values of ψ_0.
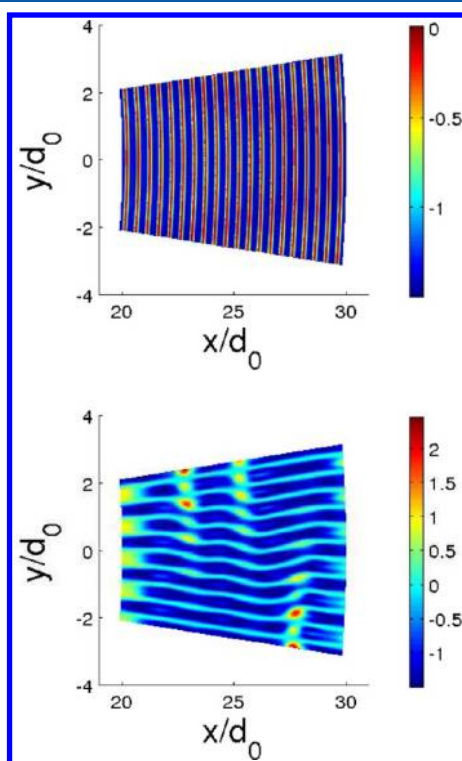

Figure 7. Polymer free energy density in the concentric (a) and radial (b) phases normalized by the absolute bulk average energy density $k_B T \tau^2 / u$. The radii are $R_1 = 20d_0$ and $R_2 = 30d_0$, $M = 747$ (a) and $M = 1328$ (b) and other parameters are as in Figure 3.
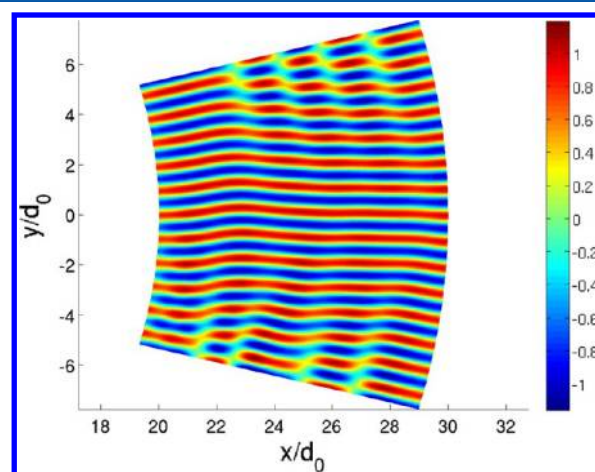

Figure 8. BCP composition in the radial phase in a wedge of 30°. The radii are $R_1 = 20d_0$ and $R_2 = 30d_0$, $M = 2075$, and other parameters are as in Figure 3.

curved and stabilized due to the curvature of the bounding surfaces. This finite-wavelength instability is different from the long-wavelength instability Onuki and Fukuda predicted for an elastic lamellar stack.[24] Another difference is that here the interfacial undulations are found in addition to a dielectrophoretic enrichment of the A monomers near the inner cylinder, as is clearly seen in Figure 10 (note the different colors at the inner and outer radii).

To better quantify these undulations we define a second order parameter

$$D^\theta = \frac{1}{\frac{1}{2}\Omega(R_2{}^2 - R_1{}^2)\phi_0{}^2} \int_{R_1}^{R_2} r \, dr \int_{\theta}^{\theta+d\theta} \left(\frac{\partial\phi}{\partial\theta}\right)^2 d\theta'$$

$$(30)$$

modulations in the azimuthal direction have the same wavelength as the lamellar thickness d_0. This behavior is reminiscent of the instability in thin-film BCPs in electric fields[9,13] although in that work the lamellae were stabilized by interfacial interactions with a flat substrate whereas here the lamellae are
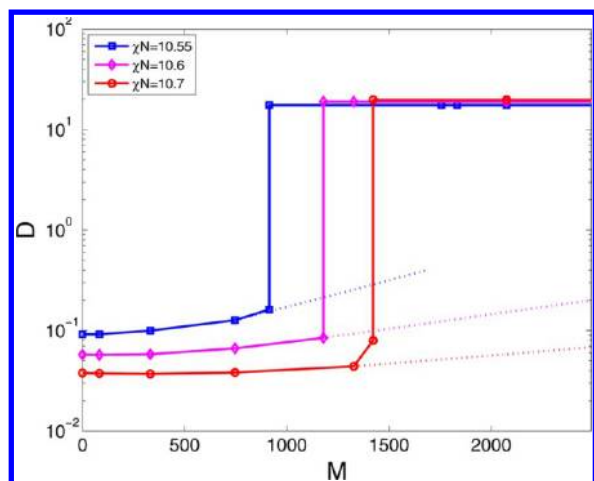
Figure 9. Orientational order parameter D from eq 29 vs M at different values of χN. Note the log scale on the vertical axis − D values of the radial phase are 2 orders of magnitude larger than in the concentric phase. The dotted lines represent solutions of concentric
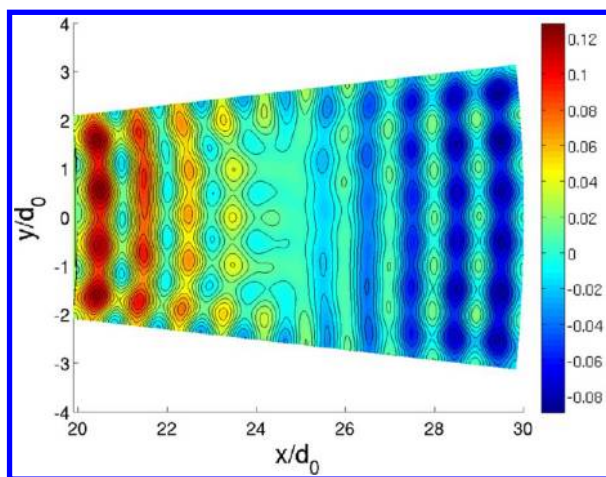

Figure 10. Interfacial undulations at large potentials. Colors represent $(\phi - \phi_0 \cos (q_0 r))/\phi_0$.

dθ is a small constant that we chose to be d$\theta = 0.1°$. Figure 11 shows how D^θ depends on the segregation (a) and on the voltage (b). The undulations are clearly more pronounced for
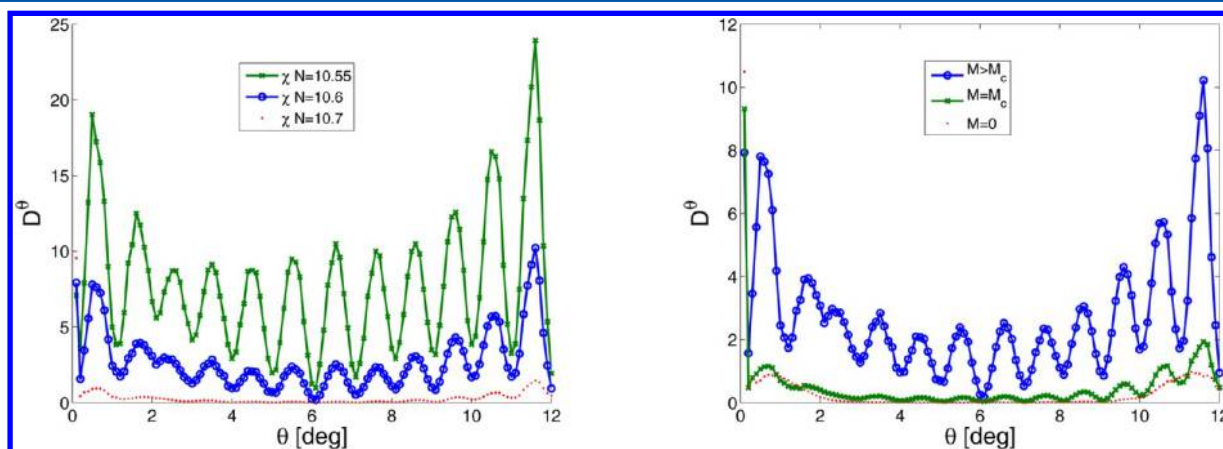
voltages ψ_0 equal to or exceeding the critical voltage ψ_c. In addition, the undulations are stronger for weaker segregations (lower values of χN) where the lamellae are easier to deform (cf. Figure 11a).

3. STRONG SEGREGATION CALCULATIONS

We consider the strong segregation limit of the competing concentric and radial phase in a cylindrical capacitor. The main contributions to the free energy of this system are the electrostatic energy difference and the free energy difference due to stretched chains.

While the free energy contribution from the electrostatic effects should favor the radial phase, the concentric phase is favored in absence of an external potential because the chain stretching energy of the radial phase outweighs the lamella-bending energy of the concentric phase.

3.1. Electrostatic energy. The electrostatic free energy of a cylindric wedge with opening angle Ω and height H is

$$F_{es}(\text{con}) = \frac{1}{2} \int \epsilon \mathbf{E}^2 \, d^3\mathbf{r} = \frac{\Omega}{2} H \int \epsilon \mathbf{E}^2 r \, dr \tag{31}$$

The two lamellar phases have the dielectric constants $\tilde{\epsilon}_1$ and $\tilde{\epsilon}_2$ in the A and B block with the difference $\Delta\tilde{\epsilon} = \tilde{\epsilon}_1 - \tilde{\epsilon}_2$. In the investigated case the external potential ψ_0 is fixed, so the charge density of the capacitor has to be computed first. The Gauss's law for a cylindric wedge with opening angle Ω is

$$\oint \mathbf{D} d\mathbf{A} = \epsilon \mathbf{E} A = E(\Omega r H) = \frac{\lambda H}{\tilde{\epsilon} \epsilon_0} \tag{32}$$

The potential difference in a ring follows from

$$\Delta\psi = \int_{r_i}^{r_o} \frac{\lambda}{\Omega \tilde{\epsilon} \epsilon_0} = \frac{\lambda}{\Omega \tilde{\epsilon} \epsilon_0} \ln \frac{r_o}{r_i} \tag{33}$$

with $\lambda = (Q/L)$ as the charge per unit length. To calculate the charge density the sum over all the rings needs to be calculated to obtain the value of λ for the potential ψ_0. The number of lamellae is given by $N_{l,\text{con}} = ((R_2-R_1)/d_0) - 1$. The potential difference of the concentric phase is

$$\Delta\psi_{cyl} = \sum_{n=0}^{N_{l,con}} \frac{\lambda}{\Omega \tilde{\epsilon}_1 \epsilon_0} \ln \frac{n + \frac{1}{2} + \frac{R_1}{D_0}}{n + \frac{R_1}{D_0}} + \frac{\lambda}{\Omega \tilde{\epsilon}_2 \epsilon_0} \ln \frac{n + 1 + \frac{R_1}{D_0}}{n + \frac{1}{2} + \frac{R_1}{D_0}} \tag{34}$$

Figure 11. Order parameter D^θ from (30) at (a) different values of χN and fixed $M \simeq 2700$, and (b) different values of M and fixed $\chi N = 10.6$. The blue line with circles is identical in both plots ($M \simeq 2700$), $M_c \simeq 970$ and $R_1 = 20d_0$ and $R_2 = 30d_0$.

The charge density λ of the concentric phase at a potential of ψ_0 is then

$$\lambda = \frac{\Omega\epsilon_0\psi_0}{\sum_{n=0}^{N_{l,con}} \frac{1}{\tilde{\epsilon}_1} \ln \frac{n + \frac{1}{2} + \frac{R_1}{D_0}}{n + \frac{R_1}{D_0}} + \frac{1}{\tilde{\epsilon}_2} \ln \frac{n + 1 + \frac{R_1}{D_0}}{n + \frac{1}{2} + \frac{R_1}{D_0}}} \tag{35}$$

$$= C_{con}\psi_0 \tag{36}$$

with C_{con} as the capacity of the capacitor containing the concentric phase. The electrostatic energy of the concentric phase at the applied potential ψ_0 is then

$$F_{es,con} = \frac{1}{2}\psi_0^2 C_{con} \tag{37}$$

The charge density for the radial phase is calculated using the same approach

$$\psi_0 = \frac{\lambda}{2\Omega\epsilon_0} \ln \frac{R_2}{R_1}\left(\frac{1}{\tilde{\epsilon}_1} + \frac{1}{\tilde{\epsilon}_2}\right) \tag{38}$$

$$\lambda = \frac{\psi_0 2\Omega\epsilon_0}{\ln \frac{R_2}{R_1}\left(\frac{1}{\tilde{\epsilon}_1} + \frac{1}{\tilde{\epsilon}_2}\right)} = C_{rad}\psi_0 \tag{39}$$

so the electrostatic energy of the radial phase follows as

$$F_{es,rad} = \frac{1}{2}\psi_0^2 C_{rad} \tag{40}$$

The difference in the electrostatic free energy of the two phases is simplified using two geometric constants $K_1 = \sum_{n=0}^{N_{l,con}} \ln(n + \frac{1}{2} + R_1/D_0)/(n + R_1/D_0)$ and $K_1 = \sum_{n=0}^{N_{l,con}} \ln(n + 1 + R_1/D_0)/(n + \frac{1}{2} + R_1/D_0)$

$$\Delta F_{es} = \frac{\psi_0^2}{2}(C_{con} - C_{rad})$$

$$= \frac{\psi_0^2}{2}\Omega\epsilon_0\left(\frac{1}{\frac{1}{\tilde{\epsilon}_1}K_1 + \frac{1}{\tilde{\epsilon}_2}K_2} - \frac{2}{\left(\frac{1}{\tilde{\epsilon}_1} + \frac{1}{\tilde{\epsilon}_2}\right)\ln\frac{R_2}{R_1}}\right) \tag{41}$$

Note that $K_1 + K_2 = \ln R_2/R_1$. Substituting $\epsilon_1 = \bar{\epsilon} + \frac{1}{2}\Delta\epsilon$ and $\epsilon_2 = \bar{\epsilon} + \frac{1}{2}\Delta\epsilon$ and using a Taylor expansion with respect to $\Delta\epsilon$ leads to

$$\Delta F_{es} = \frac{\psi_0^2}{2}\Omega\epsilon_0\left(\frac{K_1 - K_2}{\left(\ln\frac{R_2}{R_1}\right)^2}\Delta\epsilon + \frac{(K_1 - K_2)^2}{\bar{\epsilon}\left(\ln\frac{R_2}{R_1}\right)^3}(\Delta\epsilon)^2 + \ldots\right) \tag{42}$$

Neglecting the higher-order terms of $\Delta\epsilon$, we obtain

$$\Delta F_{es} \approx \frac{\psi_0^2}{2}\Omega\epsilon_0\left(\frac{K_1 - K_2}{\left(\ln\frac{R_2}{R_1}\right)^2}\right)\Delta\epsilon \tag{43}$$

3.2. CHAIN STRETCHING

To derive the difference of the free energy due to chain stretching it is usefull to look at the free energy of a brush first. We compute the free energy of the copolymer system as two brushes that are fixed to the domain boundaries of the blocks. The free energy of a brush is

$$\frac{f_e}{k_BT} = \frac{3\pi^2}{8R^2}\frac{1}{L}\int dz\, z^2 = \frac{\pi^2}{8R^2}L^2 \tag{44}$$

A planar lamellar phase has a free energy of

$$\frac{f}{k_BT} = \frac{F}{nk_BT} = \tilde{f}_e + \tilde{f}_i \tag{45}$$

with $\tilde{f}_e$ denoting the elastic free energy and $\tilde{f}_i$ the interphase free energy of a chain.

$$\tilde{f}_e = \frac{\pi^2}{8\frac{R^2}{2}}\left(\frac{D}{4}\right)^2 2 = \frac{\pi^2}{32}\left(\frac{D}{R}\right)^2 \tag{46}$$

with $R^2/2$ as the chain extension of the A segment of a copolymer chain, the thickness of the according copolymer block is $L = D/4$ so that 2 of these blocks form a lamellae and the resulting periodicity is $D = 4L$. The internal free energy is

$$\tilde{f}_i = \frac{\gamma\Sigma}{k_BT} = \frac{k_BT\sqrt{N}}{k_BTR_e^2}\sqrt{\chi N/6}\frac{2N}{\rho_0 D} = 2\frac{R_e}{D}\sqrt{\chi N/6} \tag{47}$$

with $\sqrt{N} = \frac{\rho_0 R^3}{N}$. A minimization of $f(D)/(k_BT)$ with respect to D yields the equilibrium spacing

$$D_0 = 2\left(\frac{8\chi N}{3\pi^4}\right)^{1/6}R_e \tag{48}$$

and backsubstituting into $f(D)$ yields

$$\tilde{f}_0 = \frac{f(D_0)}{k_BT} = \frac{1}{4}(9\pi^2\chi N)^{1/3} \tag{49}$$

for the free energy of an unperturbed lamellar phase.

3.2.1. Concentric Lamellar Phase. We treat the copolymer chains as brushes that are anchored at the phase interface. The chains stretch into half of the diameter (d_+/d_-) of the domains. This would lead to a reduced volume of the inner ring and an increased volume of the outer ring. Starting from a lamella with the domain boundary at radius $r = R$, for a cylindric wedge with opening angle ϕ, we obtain

$$A_+ = \frac{1}{2}\phi[(R + d_+)^2 - R^2] = \frac{1}{2}\phi[2d_+R + d_+^2] \tag{50}$$

$$A_- = \frac{1}{2}\phi[R^2 - (R - d_-)^2] = \frac{1}{2}\phi[2d_-R - d_-^2] \tag{51}$$

As the system is incompressible we equate the two areas A_+ and A_- to ensure equal volume for the blocks

$$2d_+R + d_+^2 = 2d_-R - d_-^2 = \frac{N}{\rho_0}R \tag{52}$$

leading to

$$d_\pm = \mp R \pm R\sqrt{1 \pm \frac{N\sigma}{\rho_0 R}} \tag{53}$$

The elastic free energy is then the sum of the contributions from the two blocks

$$\tilde{f}_{e+} = \frac{3\pi^2}{8}\frac{1}{R^2/2}\frac{1}{A_+}\phi\int_R^{R+d_+} dr\, r(r - R)^2 = \frac{\pi^2}{4}\left(\frac{d_+}{R_e}\right)^2\frac{1 + \frac{3}{4}\frac{d_+}{R}}{1 + \frac{1}{2}\frac{d_+}{R}} \tag{54}$$

$$\tilde{f}_{e-} = \frac{\pi^2}{4}\left(\frac{d_-}{R_e}\right)^2 \frac{1 - \frac{3}{4}\frac{d_-}{R}}{1 - \frac{1}{2}\frac{d_-}{R}} \tag{55}$$

$$\tilde{f}_e = \tilde{f}_{e+} + \tilde{f}_{e-} \tag{56}$$

Expanding the result to order $1/R^2$ and using the values for $d_\pm$ from (53), leads to

$$\tilde{f}_e = \frac{\pi^2}{4}\left(\frac{d}{R_e}\right)^2\left(1 + \frac{1}{8}\left(\frac{d}{R}\right)...\right)\cdot 2 \tag{57}$$

The interfacial free energy is

$$\tilde{f}_i = \frac{dR_e}{N}\sqrt{\chi N/6} \tag{58}$$

with $d = ((N\sigma)/(2\rho_0))$, leading to

$$\tilde{f} = \frac{\pi^2}{2}\left(\frac{d}{R_e}\right)^2\left(1 + \frac{1}{8}\left(\frac{d}{R}\right)^2 - ...\right) + \frac{R_e}{2d}\sqrt{\chi N/6} \tag{59}$$

Now $\tilde{f}$ is minimized with respect to d

$$\frac{\partial\tilde{f}}{\partial d} = \frac{d\pi^2}{R_e^2}\left(1 + \frac{1}{8}\left(\frac{d}{R}\right)^2 + ...\right) + \frac{\pi^2}{2}\left(\frac{d}{R_e}\right)^2\frac{1}{4}\frac{d}{R^2}\frac{R_e}{2d^2}\sqrt{\chi N/6} = 0 \tag{60}$$

$$\frac{d}{R_e} = \left(\frac{\chi N}{24\pi^4}\right)^{1/6}\left(1 - \frac{1}{4}\left(\frac{\chi N}{24\pi^4}\right)\left(\frac{R_e}{R}\right)^2 + ...\right) \tag{61}$$

and resubstituted into $\tilde{f}$ to obtain

$$\tilde{f} = \frac{\pi^2}{2}\left(\frac{d}{R_e}\right)^2\left(1 + \frac{1}{8}\left(\frac{d}{R}\right)^2 + ...\right) + \frac{R_e}{2d}\sqrt{\chi N/6} \tag{62}$$

$$= \tilde{f}_0\left(1 + \frac{1}{4}\left(\frac{d}{R}\right)^2 + ...\right) \tag{63}$$

with $d = R_e ((\chi N)/(24\pi^4))^{1/6}$, the lamellar periodicity is $D_0 = 4d = 2R_e ((8\chi N)/(3\pi^4))^{1/6}$. Now we average over the concentric lamellar phase and obtain

$$\tilde{f}_{con} = \tilde{f}_0 \frac{1}{\pi(R_2^2 - R_1^2)}\int_{R_1}^{R_2} dr\, r2\pi\left(1 + \frac{1}{4}\frac{d^2}{r^2} + ...\right) \tag{64}$$

$$= \tilde{f}_0\left(1 + \frac{1}{2}\frac{d^2}{R_2^2 - R_1^2}\ln\frac{R_2}{R_1} + ...\right) \tag{65}$$

3.2.2. Radial Lamellar Phase. The radial phase consists of perfectly radial lamellae with an opening angle of ϕ_0. The width of the lamellae is a function of the radius $d(r) = r\phi_0$, $\Sigma d\rho_0 = (N/2)$ or $\Sigma = ((N)/(2\rho_0\phi_0 r))$. The elastic free energy follows from

$$\tilde{f}_e = 2\frac{3\pi^2}{8}\frac{1}{R^2/2}\frac{\int_{R_1}^{R_2} r\, dr \int_0^{\phi_0} d\phi(r\phi)^2}{\int r\, dr \int d\phi} \tag{66}$$

$$= \frac{\pi^2}{4R_e^2}\phi_0^2(R_2^2 + R_1^2) \tag{67}$$

The interfacial energy is

$$\tilde{f}_i = \frac{\gamma\overline{\Sigma}}{k_B T} = \sqrt{\chi N}\frac{R_e}{R_2 + R_1}\frac{1}{\phi_0} \tag{68}$$

Now $\tilde{f}$ is minized with respect to ϕ_0, $(\partial\tilde{f}/\partial\phi_0) = 0$ leading to

$$\phi_0^3 = \sqrt{\frac{2\chi N}{4\pi^4}}\frac{R_e^3}{(R_2 + R_1)(R_2^2 + R_1^2)} \tag{69}$$

Backsubstituting this into $\tilde{f}$ gives rise to

$$\tilde{f}_{rad} = \frac{1}{4}(9\pi^2\chi N)^{1/3}\left(\frac{2(R_2^2 + R_1^2)}{(R_2 + R_1)^2}\right)^{1/3} \tag{70}$$

$$= \tilde{f}_0\left(\frac{2(R_2^2 + R_1^2)}{(R_2 + R_1)^2}\right)^{1/3} \tag{71}$$

3.3. Critical Potential. The critical potential arises from the competition between the electrostatic and the elastic free energy.

$$\Delta F_{es} - \Delta F_{el} = 0 \tag{72}$$

$$\frac{\Delta F_{es}}{k_B T} = \frac{\psi_0^2\Omega\epsilon_0}{2k_B T}\left[\frac{K_1 - K_2}{\left(\ln\frac{R_2}{R_1}\right)^2}\right]\Delta\varepsilon \tag{73}$$

$$\frac{\Delta F_{el}}{k_B T} = \frac{\rho_0\Omega\tilde{f}_0}{k_B T}\left[\left(1 + \frac{1}{2}\frac{d^2}{R_2^2 - R_1^2}\ln\frac{R_2}{R_1}\right) - \left(\frac{2(R_2^2 + R_1^2)}{(R_2 + R_1)^2}\right)^{1/3}\right] \tag{74}$$

Defining two geometric constants for the elastic and electrostatic free energy $G_{es} = [(K_1 - K_2(\ln(R_2/R_1)))]$ and $G_{el} = [(1 + (1/2)(d^2)/(R_2^2 - R_1^2) \ln (R_2/R_1)) - ((2R_2^2 + R_1^2)/(R_2 + R_1)^2)^{1/3}]$ we obtain

$$\psi_0^2 = \frac{2\rho_0 G_{el}\tilde{f}_0}{\epsilon_0 G_{es}\Delta\varepsilon} \tag{75}$$

Neglecting the influence of the geometric constrains, we obtain for the dependence of the critical potential in a first approximation

$$\psi_c \propto \frac{\sqrt{\tilde{f}}}{\sqrt{\Delta\tilde{\epsilon}}} \propto \frac{(\chi N)^{1/6}}{\sqrt{\Delta\tilde{\epsilon}}} \tag{76}$$

To compare the critical potential obtained for the strong segregation limit we use the parameters from the coarse-grained model we describe in the following section ($R_1 = 5D_0$, $R_2 = 10D_0$, $D_0 = 0.96R_e$, $k_B T = 1$, $\Delta\epsilon = 3$, $\chi N = 53.6$, chain density $\rho_0 = (128)/(R_e^3)$). The critical potential derived from this calculation is $\psi_0 \approx 16.639$ ($G_{es} = 4.611 \times 10^{-2}$, $G_{el} = 3.5742 \times 10^{-2}$, $\tilde{f}_0 = 4.20625$).

4. SOFT, COARSE-GRAINED MODEL AND SIMULATION TECHNIQUE

In order to obtain more detailed information on the polymer conformations in external fields, to extend the calculations to the practically important regime of intermediate segregation, $\chi N > 20$, and to study the kinetics of self-assembly, we use particle-based simulations. As the system size needs to be sufficiently large to contain multiple periods of the lamellar

phase, we employ a highly coarse-grained model with soft interactions that has been shown to efficiently model block copolymer phases.

The block copolymer is represented as a chain of $N = 32$ beads. The bonded interactions of beads are represented as harmonic springs

$$\frac{H_b}{k_B T} = \sum_{i=0}^{N_i} \sum_{s=1}^{N} \frac{3(N-1)}{2R_{e0}^2} (\mathbf{r}_i(s) - \mathbf{r}_i(s+1))^2 \tag{77}$$

with R_{e0} being the mean-squared end-to-end distance of a Gaussian chain R_{e0} in the absence of nonbonded interactions. It sets the unit of length. $\mathbf{r}_i(s)$ denotes the position of the sth coarse-grained segment of polymer i, N_i the number of polymer chains.

The nonbonded interactions consist of contributions from the repulsion of unlike blocks expressed by the Flory–Huggins parameter χN, the inverse isothermal compressibility κN, surface interactions and the energy of the electric field. The nonbonded polymer interactions take the form

$$\frac{H_{nb}}{k_B T} = \rho R_{e0}^3 \int \frac{d\mathbf{r}}{R_{e0}^3} \left[\frac{\kappa N}{2} (\hat{\phi}_A(\mathbf{r}) + \hat{\phi}_B(\mathbf{r}) - 1)^2 \right.$$
$$\left. - \frac{\chi N}{4} (\hat{\phi}_A(\mathbf{r}) - \hat{\phi}_B(\mathbf{r}))^2 \right] \tag{78}$$

The first term limits fluctuations of the total density and in accord with previous studies we use $\kappa N = 107.2$. The second term describes the repulsive interaction between unlike segment species and the strength is parametrized by the Flory–Huggins parameter, $\chi N = 53.6$.

The microscopic volume fraction of A segments is defined by

$$\hat{\phi}_A(\mathbf{r}) = \frac{1}{\rho N} \sum_{i=1}^{N_i} \sum_{s=1}^{Nf} \delta(\mathbf{r} - \mathbf{r}_i(s)) \tag{79}$$

where $f = 1/2$ denotes the fraction of A segments on the diblock copolymers. A similar expression holds for the local, microscopic density of B segments, $\hat{\phi}_B(\mathbf{r})$. Although the particle-based system is compressible, the normalization of the volume fraction is chosen such that $\langle \hat{\phi}_A(\mathbf{r}) \rangle = f$ and $\langle \hat{\phi}_B(\mathbf{r}) \rangle = 1 - f$.

To align phases to the surface an additional contribution to the Hamiltonian is used:

$$\frac{H_{wall}}{k_B T} = \rho R_{e0}^3 \int \frac{d\mathbf{r}}{R_{e0}^3} N U_W(\mathbf{r})(\hat{\phi}_A(\mathbf{r}) - \hat{\phi}_B(\mathbf{r})) \tag{80}$$

The coupling between the morphology of the copolymers and the electric field is achieved via the composition-dependent permittivity $\epsilon(\phi(\mathbf{r}))$ appearing in the Hamiltonian of the electric field, (3). The Laplace equation for the electric field, (8), is a homogeneous partial differential equation since the system does not contain charges. It can be rewritten as

$$\nabla \epsilon(\mathbf{r}) \cdot \nabla \psi(\mathbf{r}) + \epsilon(\mathbf{r}) \nabla^2 \psi(\mathbf{r}) = 0 \tag{81}$$

to show the difference from the common problem of Laplace's equation in a uniform medium.

Since a microscopic expression for the permittivity of a polymer mixture is lacking, we choose two linear approximations, a density-dependent and a density-independent form. The density-independent form

$$\epsilon(\mathbf{r}) = \frac{\epsilon_0}{\hat{\phi}_A(\mathbf{r}) + \hat{\phi}_B(\mathbf{r})} (\epsilon_A \hat{\phi}_A(\mathbf{r}) + \epsilon_B \hat{\phi}_B(\mathbf{r})) \tag{82}$$

does not couple the polymer density to the electric potential and it will not result in the vacuum permittivity in the absence of polymer. For dense phases, as used in this study, this density-independent form turned out to be well suited. Alternatively, a density-dependent form

$$\epsilon(\mathbf{r}) = \epsilon_0(1 + \hat{\phi}_A(\mathbf{r})(\epsilon_A - 1) + \hat{\phi}_B(\mathbf{r})(\epsilon_B - 1)) \tag{83}$$

would include density effects caused by the external electric potential in a first approximation, but due to the finite compressibility of the particle-based model extra care needs to be taken at the surface, where there are steep density gradients.[25] As the soft-coarse grained model has a slightly increased density at the inner electrode, the electric field solution deviates slightly from the first approach. Figure 12 shows the density distribution
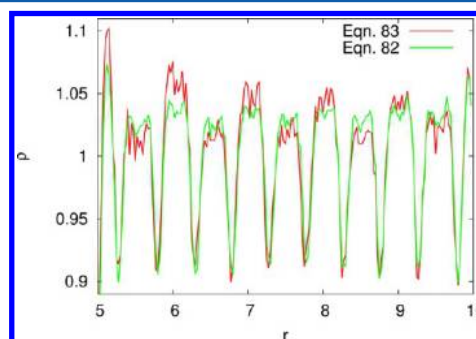

Figure 12. Density profile of a concentric lamellar configuration in an electrical field below the critical potential with the two different constitutive equations eq 82 and eq 83. The density dependent equation leads to an increase of density at the inner electrode. To avoid this effect the density independent constituitive eq 82 was chosen.

in a typical concentric case. Using the density-dependent constituitive equation leads to a higher permittivity and thus weaker fields at the inner electrode.

In a more detailed model, other approaches to calculate the dielectric constant of the polymer mixture could be applied, especially by taking into account polarizabilities.[26] Our model relies on a discretization of the fields for density and order parameter. A more accurate dielectric constant calculation would have aliasing effects caused by this discretization as well. As we mainly focus on universal consequences of an inhomogeneous field for large scale morphologies we chose a simple approach for this matter. A better approximation to the dielectric function will most likely not influence the qualitative results of our method.

The permittivity of the pure phases A and B is set to $\tilde{\epsilon}_A = 5$ and $\tilde{\epsilon}_B = 2$.

In this scheme, we rewrite the Laplace equation as

$$\frac{\epsilon_0 \overset{*}{\tilde{\psi}}}{R_e^2} (R_e \nabla)[\tilde{\epsilon}(R_e \nabla)\tilde{\psi}] = 0 \tag{84}$$

The electric potential ψ is then $\psi = \tilde{\psi}\psi^* = \tilde{\psi}(k_B T / \epsilon_0 Re)^{1/2}$. The dimensionless parameter $\tilde{\psi}$ is related to M via $M = \tilde{\psi}^2/2$. The electrostatic potential is set to values in the range of $\tilde{\psi} = 1-50$.

The statistical mechanics of the soft, coarse-grained particle-based model is studied by Single-Chain-in-Mean-Field (SCMF) simulations.[27−29] This method is the Monte Carlo analogue to the multiple time step algorithm in molecular dynamics[30] with a grid-based instead of pairwise computation of nonbonded

interactions. This computational strategy is particular advantageous in the presence of long-range electrostatic interactions.

In a conventional Monte Carlo simulation, the electric field has to be recomputed for accepting every trial move and thereby causing huge computational effort. In SCMF simulations, however, we temporarily replace the weak, nonbonded interactions, including the compute-intensive long-range electrostatic ones, by external fields. The polymer configurations are updated by Metropolis Monte Carlo using Smart Monte Carlo moves. For every move a bead is picked randomly, the forces acting on the bead are computed from the strong bonded Hamiltonian. The trial move is adjusted by this force bias to increase the acceptance ratio[31] and fulfill the detailed balance . The local random displacement of segments give rise to Rouse-like dynamics. The chain relaxation time τ_0 is characterized by the time the center of mass of a macromolecule takes to diffuse a distance of the actual end-to-end distance $R_e = 1.02R_{e0}$, $\tau = R_e^2/D = 9711$ Monte Carlo-steps.

The nonbonded contributions, including the electrostatic potential, are updated once per Monte Carlo step, which consists of Nn trial moves, with Nn being the number of particles in the simulation and thus giving every particle the chance to be moved once per Monte Carlo step.

5. COMPUTATIONAL DETAILS

The simulation within the SCMF framework requires solving the Laplace equation at every update of the fields that are used to compute the nonbonded interactions. As it was crucial to find a solution for this problem that operates at a speed of the same order of magnitude as the overall MC simulation, we describe the computational method in more detail. The permittivity $\epsilon(\mathbf{r})$ and the electrostatic potential $\psi(\mathbf{r})$ are defined on a collocation grid. The grid spacing is $R_e/6$ and for each grid cell the densities, $\hat{\phi}_A(\mathbf{r})$ and $\hat{\phi}_B(\mathbf{r})$, are computed from the number of particles residing in that cell. The Laplace equation is discretized with a second order finite differences scheme leading to a homogeneous system of linear equations. Defining the corresponding matrix elements to write the equation in terms of a matrix-vector product requires a some derivations as the three-dimensional periodic fields of permittivity and electrostatic potential are mapped to a one-dimensional vector. To simplify, we specify one element of the second order finite differences stencil defining a Jacobi-step. The potential $\psi_{i+1}(r)$ follows from the potential $\psi_n(r)$ using relative coordinates $x \pm 1$ as follows

$$\psi_{i+1}(r) = \frac{\frac{1}{4}[\epsilon(r_{x+1}) - \epsilon(r_{x-1})] + \epsilon(r)}{6\epsilon(r)}\psi_i(r_{x+1}) + \ldots \tag{85}$$

The other five contributions are defined accordingly. For a system with constant permittivity this converges to the standard stencil for Laplacian differential equations

$$
\begin{aligned}
&\psi(r) \\
&= \frac{\psi(r_{x+1}) + \psi(r_{x-1}) + \psi(r_{y+1}) + \psi(r_{y-1}) + \psi(r_{z+1}) + \psi(r_{z-1})}{6}
\end{aligned}
\tag{86}
$$

From this the $6N$ coefficients of a sparse matrix M can be derived that defines the system of linear equations as $Mx = 0$. A conjugate-gradient solver is used to iteratively solve this problem and is shortly described in this section. Given the nth estimate of the solution x_n, a residual r_n is calculated from $r_n = -Mx_n$. The square modulus of the residual is used as accuracy criterion $|r_n|^2/n_{grid}$. Initially the search direction is defined by first residual $s_0 = r_0$, following search directions s_n are calculated to be orthogonal to the previous search direction. After determining the search direction s_n a step length α is computed from a quadratic minimization of the residual

$$\alpha = \frac{r_n \cdot Ms_n}{|M\rho_n|^2} \tag{87}$$

and the $(n + 1)$th estimate is calculated from the nth estimate as

$$x_{n+1} = x_n + \alpha s_n \tag{88}$$

The Laplace solver is parallelized using a simple domain decomposition MPI scheme with a synchronization after each iteration step. The advantage of this iterative method is that because of the small changes in the configuration only a few conjugate gradient steps are needed to converge to the desired accuracy of the solution, for practical reasons this accuracy was chosen to be $|r_n|^2/n_{grid} < 10^{-3}$.

The systems are typically set up with a random distribution of copolymer beads, which is equivalent to an isotropic, disordered melt at $\chi N = 0$. This initial state corresponds to a rapid cooling of the copolymer melt below the ODT temperature. For the cases of concentric lamellae a square well potential in form of concentric rings with a depth of $1k_BT$ a width of $d_0/2$ and a periodicity of d_0 acting on one of the copolymer components was used during the equilibration period to enforce a defect-free ordering. After the initial alignment the potential was switched off and the system was allowed to evolve freely for 50 000 Monte Carlo steps ($\approx 5\tau_0$), in which the concentric lamellar structure was retained. To avoid effects on the electrostatic potential due to the walls, a concentric wedge is placed in a rectangular box and the electrostatic potential is solved in the entire box. It is set to the exact solution of a cylindrical capacitor at the walls of the simulation domain. The electrodes have a constant potential. The dielectric constant of the material outside the accessible area is set to be $(\epsilon_A + \epsilon_B)/2$. Figure 13 illustrates a typical solution of the Laplace equation.
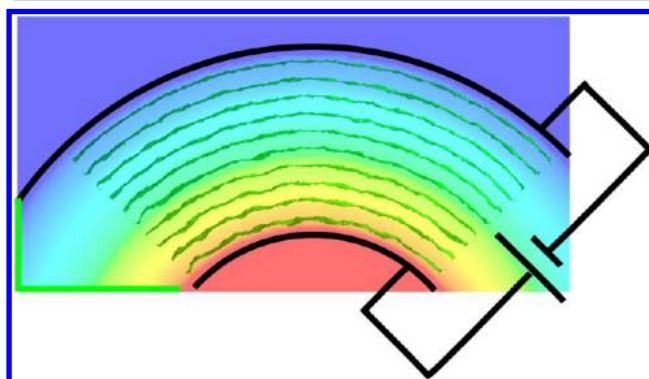

Figure 13. Electric potential as computed by the SCMF electrostatics solver. The plain blue and red areas are the electrodes with a fixed potential. The electrostatic potential is semitransparent to allow the observation of the wedge filled with copolymer. To indicate the area containing copolymer the domain interfaces are shown by a green isosurface. The Laplace equation is solved for the entire area except the electrodes and the walls. The green lines indicate the wall area that has a fixed electric potential derived from the exact solution of a cylindrical capacitor. The potential used in this case is $\tilde{\psi} = 16$ ($M = 128$).

6. CONCENTRIC COPOLYMER PHASES

To obtain a concentric phase as predicted by the 2D phase diagram a cylindrical wedge with radial walls in the absence of an external field was simulated. A surface potential in form of a square well with a depth of $1k_BT$ and a width of $R_{e0}/6$ acting on the A component was used at the walls to induce a concentric phase in their vicinity. This surface potential was used during the entire simulation. We consider two different thicknesses H of the simulation cell, $1d_0$ and $(3/2)d_0$, using 75 108 chains of 32 beads for the first and 112 662 chains for the second configuration, respectively. This gives rise to a constant density of $\sqrt{\bar{N}} = 128$ chains per unit volume. The thickness was
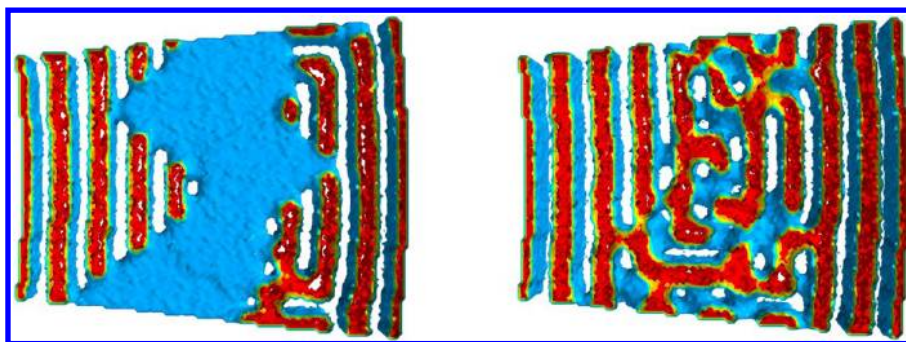
Figure 14. Cylindrical system segment, $H = 1d_0$ (left) and $H = 3/2d_0$ (right), $R_1 = 30d_0$, $R_2 = 40d_0$, concentric lamellae form due to contact potential at the inner and outer ring. As soon as the periodicity in z allows lamellae perpendicular to the axis, they are formed in the inner part of the system where the influence of the wall potential is low. Even though in the case of $H = 1.5d_0$ the concentric lamellae phase has the lowest energy, the region in the middle of the simulation retains some defects.
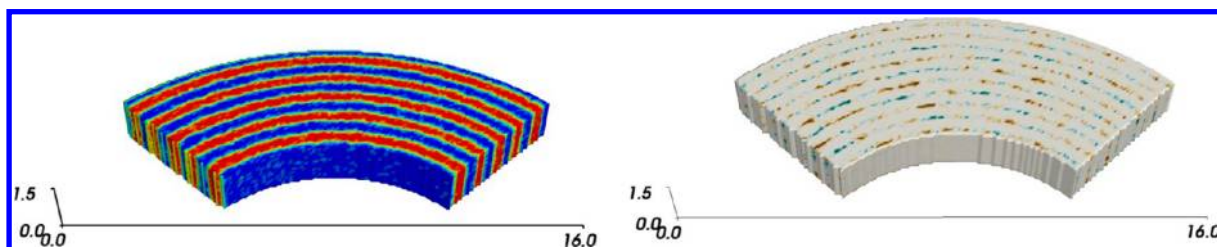

Figure 15. Cylindrical system segment showing a metastable concentric phase (left) and the difference $\Delta\phi = \phi_{start} - \phi_{end}$ of the order parameter to the generated perfect concentric arrangement after an equilibration of 50 000 steps ($\approx 5\tau_0$)(right).

commensurate with a lamellar stacking in the first case and incommensurate in the second case thus inhibiting the formation of lamellae parallel to the plane of the slab. For $h = (3/2)d_0$, the slightly bent concentric lamellar phase presumably is the lowest free energy configuration of this system, but the energy differences are minuscule and the simulation does not reach perfect alignment even after a long time (200 000 Monte Carlo steps $\approx 20\tau_0$) as can be seen in Figure 14. The effect of a surface potential on the phase diagram of a block copolymers has been studied before.[32−34] Our observations agree with the general effect of a surface potential on a block copolymer alignment − the ordering influence vanishes after a few lamellar spacings.

To approach the problem from the opposite side, a system with a high concentric curvature and prealigned copolymer was prepared by forcing the copolymer into position with the previously described ring potential. The height was chosen to be $H = 3/2d_0$. After equilibration, the external field was switched off and the copolymer was allowed to evolve freely for 100 000 steps corresponding to a time of $\approx 10\tau_0$. Figure 15 shows the final configuration and the difference of the order parameter to the starting configuration. Only small fluctuations of the local interface positions are detectable but no indication of a morphology transformation are visible. This demonstrates the high free energy barriers between the concentric phase and the radial phase.

7. ALIGNING TO EXTERNAL ELECTRIC FIELDS

To demonstrate that the electric field can produce an ordered lamellar phase at intermediate segregation we consider a cylindrical wedge with neutral walls. The inner and outer radii are defined in units of the lamellar spacing d_0 with $d_0 = 1.92R_{e0}$, $R_1 = 5d_0$, $R_2 = 10d_0$ and the opening angle is $\Omega = \pi/2$. The system is periodic in the direction of the cylinder axis.

The height H was set to be incommensurate with a lamellar stacking perpendicular to the cylinder axis ($H = (3/2)d_0$). The final configuration of the simulation is depicted in 16 after 50 000 steps, corresponding to $\approx 5\tau_0$. The system is fully ordered by the electric field, most of the polymer interfaces are parallel to the field, which is the lowest energy state. The periodicity in the z-direction is incommensurate with lamellae perpendicular to the cylinder axis, the systems uses the extra degree of freedom to reduce the branching of lamellae by twisting them. The minimal energy state in this case is lamellae parallel to the plane of the wedge, which is formed for a system with a height of $1d_0$, as can be seen in Figure 17.

7.1. Interface Stability. As demonstrated in Figure 16, the electric field acting on the concentric lamellae results in undulations that may lead to a breakdown of the concentric phase and to ordering into the radial morphology. The innermost lamella forms undulations with increasing amplitude that lead via an intermediate T-junction motif into the radial phase. Lyakhova et al.[36] investigated pathways of reordering a lamellar system from the parallel to the perpendicular state in a plate capacitor for systems close to an order−disorder transition. The two identified pathways are via intermediate spheres and due to defect movement and rotation of the lamellae. Because of the inhomogeneity of the field in the cylindric system the transition migrates from the area with strong electric field to the area of low electric field and thus a different pathway is observed.

To investigate the influence of the electric field on the undulations, the wavelength of the undulations was measured as a function of the electric potential in a series of simulations. Lamellae closest to the inner electrode were examined after a short simulation time (500−6000 Monte Carlo steps) to capture the behavior before the breakdown of the concentric ordering. Below a critical potential no growing interfacial undulations were observed; only thermal fluctuations of the local interface position (i.e., capillary waves) were detectable.
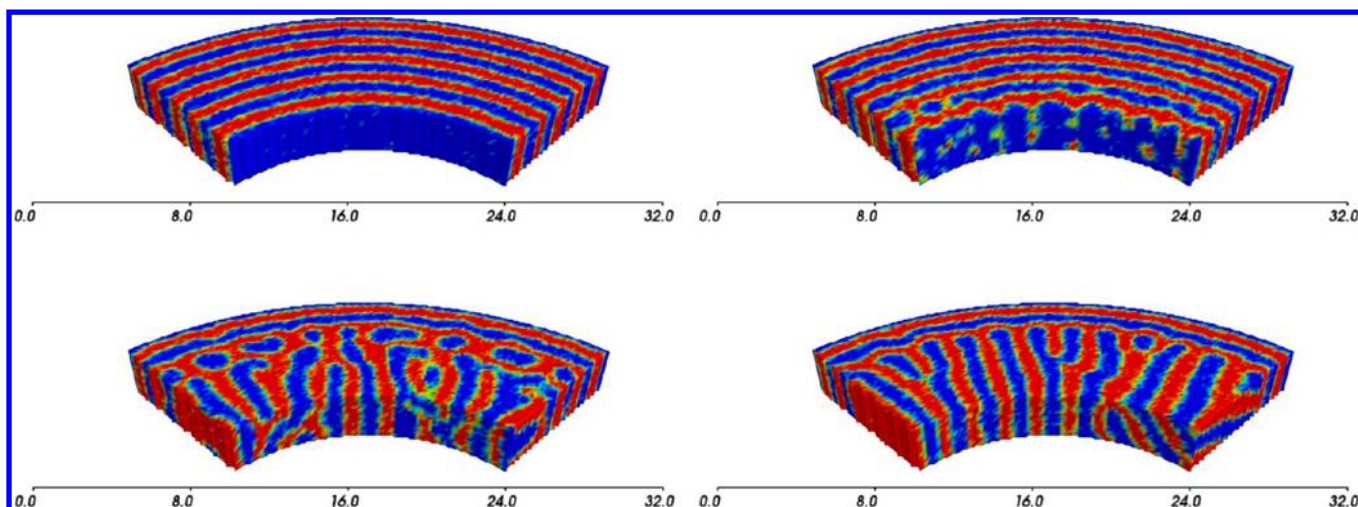
Figure 16. Reordering of a concentric lamellar system of block copolymer in an external electric field, $H = 1.5d_0$, $R_1 = 5d_0$, $R_2 = 10d_0$, $\tilde{\psi} = 36$ ($M = 648$): (left top) starting configuration of concentric lamellae, (right top) first undulations after 1000 Monte Carlo steps ($\approx 0.1\tau_0$), (left, bottom) an intermediate result after 7000 steps showing the breakdown of the lamellae in the area of the stronger electric field, and (right, bottom) the result after 70 000 steps ($\approx 7\tau_0$). Radial lamellae are enforced by the field, and lamellae branching is partially avoided by twisting and thickening of the lamellae. The height of the system is incommensurate with lamellae perpendicular to the cylinder axis. As the field falls off proportional to $1/r$, it is below the critical reordering strength at the outer lamella and the concentric structure is retained. An interesting feature is that the interface of the two competing structures form T-junction like structures, which are also observed from simulations using only surface interactions.[35]
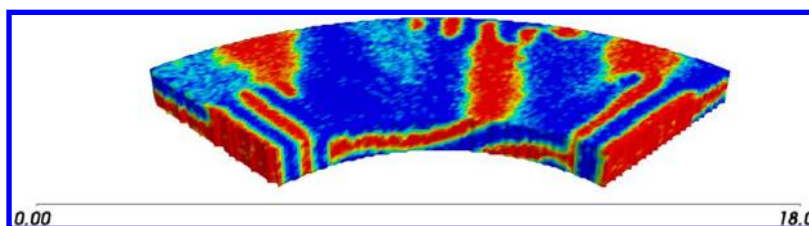

Figure 17. Result of the reordering of a concentric lamellar system of block copolymer in an external electric field, $H = d_0$, $R_1 = 5d_0$, $R_2 = 10d_0$, $\tilde{\psi} = 20$ ($M = 200$) after 50 000 steps ($\approx 5\tau_0$). The height of the system is commensurate with lamellae perpendicular to the cylinder axis.

For a quantitative analysis a series of 31 independent simulations at six electrostatic potentials ($26 \leq \tilde{\psi} \leq 36$) were undertaken and the capillary wave spectrum of the innermost lamella was analyzed. In a first approximation the capillary wave spectrum changes exponentially with time

$$S(q, t) = S(q, 0)e^{G(q)t} \tag{89}$$

with $G(q)$ being the wave-vector dependent exponential growth rate. Results for the growth rate are shown in Figure 18 and
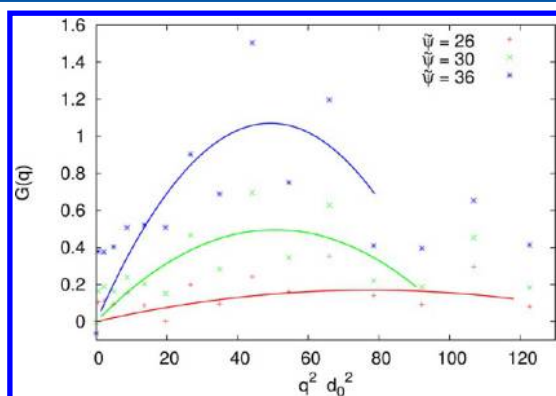

Figure 18. Wave-vector dependent growth rate $G(q)$. The points are results from simulations, the solid lines are fits of a quadratic function to help identify the wave-vector with the highest growth rate.

Table 1. Interface Undulation Wavelength as a Function of the Applied Potential from SCMF-Simulations

potential $\tilde{\psi}$	wave vector with highest growth rate/d_0	growth rate $G(q)$/step	wavelength d_0
26	8.80	0.17	0.714
28	8.56	0.34	0.734
30	7.11	0.50	0.883
32	6.94	0.71	0.906
34	7.03	0.88	0.894
36	7.03	1.07	0.894

Table 1 and the dependency of the fastest growing mode on the applied electrostatic potential is presented in Figure 19.

Since long-wavelength fluctuations of the interface are correlated with the diffusion of segments in our Monte Carlo dynamics, the growth rate vanishes like q^2. Like in spinodal decomposition of a simple binary liquid, the growth rate exhibits a maximum at finite wave vectors q_{max}. Unlike the situation in a simple binary liquid, however, q_{max} does not increase with the distance from the instability. In our system, q_{max} slightly decreases and seems to approach a constant value indicating the importance of the interactions between the internal AB interfaces and the intrisic length scale of the lamellar structure.

From Figure 19 b) the spinodal point of the electrostatic potential ($\tilde{\psi}_{spin} = 24.3$) is determined. The innermost lamella becomes unstable for higher potentials, but as can be seen from Figure 16 a potential of $\tilde{\psi} = 36$ is not sufficient to perfectly
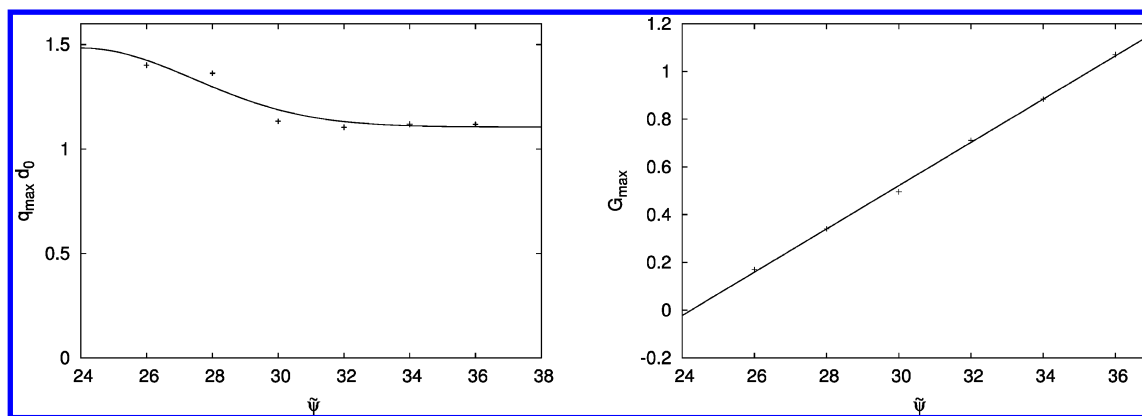
Figure 19. Dependency of the fastest growing wave-vector (left) and its growth rate (right) on the applied electrostatic potential. While the growth rate depends almost linear on the applied potential, the fastest growing wave vector is largely independent of the applied potential and reaches a plateau for larger values of $\tilde{\psi}$, the black line in the left picture is put in as a guide to the eye.

order the system into radial lamellae. The critical voltage derived from the strong segregation calculations for a first-order transition of the same system is $\tilde{\psi} = 14.68$. The spinodal point has to be at a higher potential than the phase coexistance point. In the strong segregation limit the domain boundaries are infinitely sharp, so the electrostatic energy of the concentric phase is higher. This leads to a lower transition potential for the SSL. Even though the results of these two approaches can not be compared directly they remarkably have the same order of magnitude.

8. CONCLUSIONS

We investigated lamellar phases of block copolymers confined into cylindrical pores as a model system for lamellae in non-uniform electric fields. Both the role of geometric confinement as well as the effect of a radially oriented field have been explored by 2D Ginzburg–Landau calculations in the WSL, strong segregaton calculations and 3D particle-based simulations focusing on the relative stability of the concentric vs radial lamellar phases.

In the absence of an electric field, the stability diagram, shown in Figure 2, comprises the disordered melt and concentric and radial lamellae in the $\bar{\tau}$-X plane. At a fixed geometry, given by the ratio $X = R_2/R_1$, an increase of incompatibility $|\bar{\tau}|$ or χN makes the lamellae "stiffer". The elastic energy of splay (radial lamellae) or bending (concentric lamellae) increases and at sufficiently large value of $|\bar{\tau}|$ the disordered phase is more preferential. At a fixed segregation and at small values of X, radial lamellae are stable because the system is nearly flat. As X increases the energetic cost of splay increases until it is preferential for the lamellae to bend and the concentric phase becomes more stable. At higher values of q_0R_1, i.e., at small lamellar thickness d_0, this transition from radial to concentric lamellae occurs at smaller values of X.

When the electric potential increases, concentric lamellae become less stable compared to radial ones until, at the critical voltage, radial lamellae are energetically favored (see Figures 5b and 9). An interfacial instability of concentric lamellae may appear prior to this transition, with wavelength comparable to the lamellar thickness. This instability is found both by minimization the free energy in the Ginzburg–Landau model and by particle-based simulations. The simulations also allow us to study the kinetics of this morphological transformation. In particular we calculate the wavevector q_{max} of the fastest

growing mode. We find that the growth rate depends linear on the applied potential and allows to identify easily the critical potential ψ^+ where the concentric phases ceases to be meta-stable (spinodal point). q_{max} is mostly independent of the applied potential. For potentials slightly above ψ_c, we observe a shorter wavelength of the fast growing interface undulation modes. In addition, we study the defects that develop in the confined system. These defects allow the polymer to relax some of the tension from splay and bending of the frustrated lamellae.

This is the first study of confined lamellae with inhomogeneous electric field, and we believe that the framework laid here is potentially useful to study other systems where electric and elastic forces compete. In particular, it would be interesting to investigate the static and dynamics of block copolymers in topographically and electrostatically patterned environments with the aim of directing the assembly of such systems with external fields.

■ AUTHOR INFORMATION

Corresponding Author
*(U.W.) E-mail: welling@theorie.physik.uni-goettingen.de.

Notes
The authors declare no competing financial interest.

■ REFERENCES

(1) Bates, F. S.; Fredrickson, G. H. *Phys. Today* **1999**, *52*, 32−38.
(2) Park, C.; Yoon, J.; Thomas, E. L. *Polymer* **2003**, *44*, 6725−6760.
(3) Morkved, T. L.; Lu, M.; Urbas, A. M.; Ehrichs, E. E.; Jaeger, H. M.; Mansky, P.; Russell, T. P. *Science* **1996**, *273*, 931−933.
(4) Ashok, B.; Muthukumar, M.; Russell, T. P. *J. Chem. Phys.* **2001**, *115*, 1559.
(5) Böker, A.; Elbs, H.; Hänsel, H.; Knoll, A.; Ludwigs, S.; Zettl, H.; Urban, V.; Abetz, V.; Müller, A. H. E.; Krausch, G. *Phys. Rev. Lett.* **2002**, *89*, 135502.

(6) Kyrylyuk, A. V.; Zvelindovsky, A. V.; Sevink, G. J. A.; Fraaije, J. G. E. M. *Macromolecules* **2002**, *35*, 1473−1476.

(7) Thurn-Albrecht, T.; DeRouchey, J.; Russell, T. P.; Kolb, R. *Macromolecules* **2002**, *35*, 8106−8110.

(8) Böker, A.; Elbs, H.; Hänsel, H.; Knoll, A.; Ludwigs, S.; Zettl, H.; Zvelindovsky, A.; Sevink, G.; V. Abetz, V. U.; Müller, A.; Krausch, G. *Macromolecules* **2003**, *36*, 8078−8087.

(9) Tsori, Y.; Andelman, D. *Macromolecules* **2002**, *35*, 5161−5170.

(10) Tsori, Y.; Tournilhac, F.; Leibler, L. *Macromolecules* **2003**, *36*, 5873−5877.

(11) Matsen, M. W. *Macromolecules* **2006**, *39*, 5512−5520.

(12) Matsen, M. W. *Phys. Rev. Lett.* **2005**, *95*, 258302.

(13) Matsen, M. W. *Soft Matter* **2006**, *2*, 1048−1056.

(14) Tsori, Y.; Andelman, D.; Lin, C.-Y.; Schick, M. *Macromolecules* **2006**, *39*, 289−293.

(15) Schmidt, K.; Schoberth, H. G.; Schubert, F.; Hänsel, H.; Fischer, F.; Weiss, T.; Sevink, G.; Zvelindovsky, A.; Böker, A.; Krausch, G. *Soft Matter* **2007**, *3*, 448−453.

(16) Tsori, Y. *Macromolecules* **2007**, *40*, 1698−1702.

(17) Tsori, Y. *Rev. Mod. Phys.* **2009**, *81*, 1471.

(18) Stoykovich, M. P.; Müller, M.; Kim, S. O.; Solak, H. H.; Edwards, E. W.; de Pablo, J. J.; Nealey, P. F. *Science* **2005**, *308*, 1442−1446.

(19) Daoulas, K. C.; Müller, M. *J. Chem. Phys.* **2006**, *125*, 184904.

(20) Daoulas, K. C.; Müller, M.; de Pablo, J. J.; Nealey, P. F.; Smith, G. D. *Phys. Rev. Lett.* **2006**, *96*, 036104.

(21) Leibler, L. *Macromolecules* **1980**, *13*, 1602−1617.

(22) Ohta, T.; Kawasaki, K. *Macromolecules* **1986**, *19*, 2621−2632.

(23) Fredrickson, G. H.; Binder, K. *J. Chem. Phys.* **1989**, *91*, 7265−7275.

(24) Onuki, A.; Fukuda, J. *Macromolecules* **1995**, *28*, 8788−8795.

(25) Müller, M.; Steinmüller, B.; Daoulas, K. C.; Ramirez-Hernandez, A.; de Pablo, J. *Phys. Chem. Chem. Phys.* **2011**, *13*, 10491.

(26) Nakamura, I.; Shi, A.; Wang, Z. *Phys. Rev. Lett.* **2012**, *109*, 257802.

(27) Daoulas, K. C.; Müller, M.; de Pablo, J. J.; Nealey, P. F.; Smith, G. D. *Soft Matter* **2006**, *2*, 573−583.

(28) Daoulas, K. C.; Müller, M. *J. Chem. Phys.* **2006**, *125*, 184904.

(29) Müller, M. *J. Stat. Phys.* **2011**, *145*, 967.

(30) Tuckerman, M.; Berne, B.; Martyna, G. *J. Chem. Phys.* **1992**, *97*, 1990.

(31) Rossky, P. J.; Doll, J. D.; Friedman, H. L. *J. Chem. Phys.* **1978**, *69*, 4628−4633.

(32) Milner, S.; Morse, D. *Phys. Rev. E* **1996**, *54*, 3793−3810.

(33) Hongge, T.; Dadong, Y.; Shi, A. *Macromolecules* **2004**, *37*, 9646−9653.

(34) Segalman, R. A. *Mat. Sci. Eng. R* **2005**, *48*, 191−226.

(35) Pinna, M.; Guo, X.; Böker, A.; Zvelindovsky, A. V. *ACS Nano* **2010**, *4*, 2845−2855.

(36) Lyakhova, K. S.; Zvelindovsky, A. V.; Sevink, G. J. A. *Macromolecules* **2006**, *39*, 3024−3037.

■ NOTE ADDED AFTER ASAP PUBLICATION

This article posted ASAP on February 11, 2014. Figure 12 is revised and there are numerous changes throughout the paper. The correct version posted on February 27, 2014.